



OPEN

# Graphene/Ionic Liquid Composite Films and Ion Exchange

SUBJECT AREAS:

CHEMICAL  
ENGINEERING

NANOSCALE MATERIALS

MECHANICAL ENGINEERING

Yufei Mo<sup>1,2</sup>, Yunfang Wan<sup>2</sup>, Alicia Chau<sup>2</sup> & Fuchuan Huang<sup>1</sup>

<sup>1</sup>Guangxi Key Laboratory of Petrochemical Resource Processing and Process Intensification Technology, Guangxi University, Nanning 530004, P. R. China, <sup>2</sup>School of Engineering & Applied Science, The George Washington University, Washington DC, 20052, United States.

Received  
24 October 2013Accepted  
16 May 2014Published  
27 June 2014

Correspondence and  
requests for materials  
should be addressed to  
Y.M. (yufeimo@gxu.  
edu.cn)

Wettability of graphene is adjusted by the formation of various ionic surfaces combining ionic liquid (IL) self-assembly with ion exchange. The functionalized ILs were designed and synthesized with the goal of obtaining adjustable wettability. The wettability of the graphene surface bearing various anions was measured systematically. The effect of solvent systems on ion exchange ratios on the graphene surface has also been investigated. Meanwhile, the mechanical properties of the graphene/IL composite films were investigated on a nanometer scale. The elasticity and adhesion behavior of the thin film was determined with respect to the indentation deformation by colloid probe nanoindentation method. The results indicate that anions played an important role in determining graphene/IL composite film properties. In addition, surface wetting and mechanics can be quantitatively determined according to the counter-anions on the surface. This study might suggest an alternate way for quantity detection of surface ions by surface force.

The emergence of graphene nanosheet (GN) has recently opened up an exciting new field in the science and technology of two dimensional nanomaterials with constantly growing academic and technological impetus. GN exhibits unique electronic<sup>1</sup>, optical<sup>2</sup>, magnetic<sup>3</sup>, thermal and mechanical properties<sup>4,5</sup> arising from its strictly pure carbon composition with two dimensional single layer structures<sup>6–8</sup>. Chemically converted graphene can be prepared by reduction of graphene oxide<sup>9,10</sup>, and it was expected to have various potential applications towards: field-effect transistors<sup>11,12</sup>, energy storage<sup>13,14</sup>, transparent electrodes<sup>15,16</sup>, nanocomposites<sup>17,18</sup> and biosensors<sup>19,20</sup>. There are several methods currently employed for preparing single layer graphene, such as mechanical cleavage of high-order pyrolytic graphite, chemical vapor deposition on metal surface<sup>21,22</sup>, epitaxial growth on an insulator<sup>23</sup>, reduction of single layer graphene oxide<sup>24</sup>, intercalation of graphite<sup>25</sup> etc. However, many of the methods are not suitable to make large quantities of graphene samples. Few-layer graphene can be obtained by different chemical procedures, such as thermal exfoliation of graphite oxide, reduction of graphene oxide with reducing agents such as hydrazine under microwave irradiation and solvothermal treatment of graphene oxide<sup>26,27</sup>. The most common method for preparing graphene samples in large quantities is through the reduction of its oxide. The reduction of exfoliated graphite oxide from its colloidal suspension has been proven to be an effective and reliable method of producing graphene on a large scale<sup>28</sup>. Meanwhile, there are also challenges in solvent dispersion and further chemical modification to limit the development of graphene. It often becomes necessary to prepare dispersions or solutions of graphene in organic or aqueous media. Covalent functionalization employs amidation with organic amines and interaction of organosilane and organotin reagents<sup>29</sup>. Noncovalent functionalization is achieved by wrapping graphene with surfactants or through  $\pi$ - $\pi$  interactions with aromatic molecules<sup>30</sup>.

The control of graphene surface wettability has been widely exploited in many important applications including microfluidics<sup>31</sup>, microfabrication<sup>32</sup>, drug delivery<sup>33</sup>, and stress sensor<sup>34</sup>. Diverse strategies have been developed for controlling wettability of surfaces on the basis of self-assembled monolayer (SAM) and polymeric films in response to environmental changes, such as temperature, solvent, pH, electric charge and oxidation-reduction. Previous research is mainly focused on the reorganization of the surface or internal structure and the orientation of SAMs<sup>35–37</sup>. Hereon, we present a direct ion exchange on surface of graphene/IL composite film by ionic liquid (IL) assembly. IL is low melting point salts which represent a new class of ionic media. They are composed of ion pairs containing bulky, asymmetric cations and anions. The low melting point of IL compared to classical molten salts is due to the particular chemical structure of their anions and cations.

Hybrid nanocomposite materials based on graphene and ionic liquid with unique and highly attractive properties have triggered the creation of new and future prominent applications in supercapacitor<sup>38</sup>, electrocatalyst<sup>39</sup>, microelectromechanical lubrication systems<sup>40</sup>. In this work, an ion exchange on the graphene surface

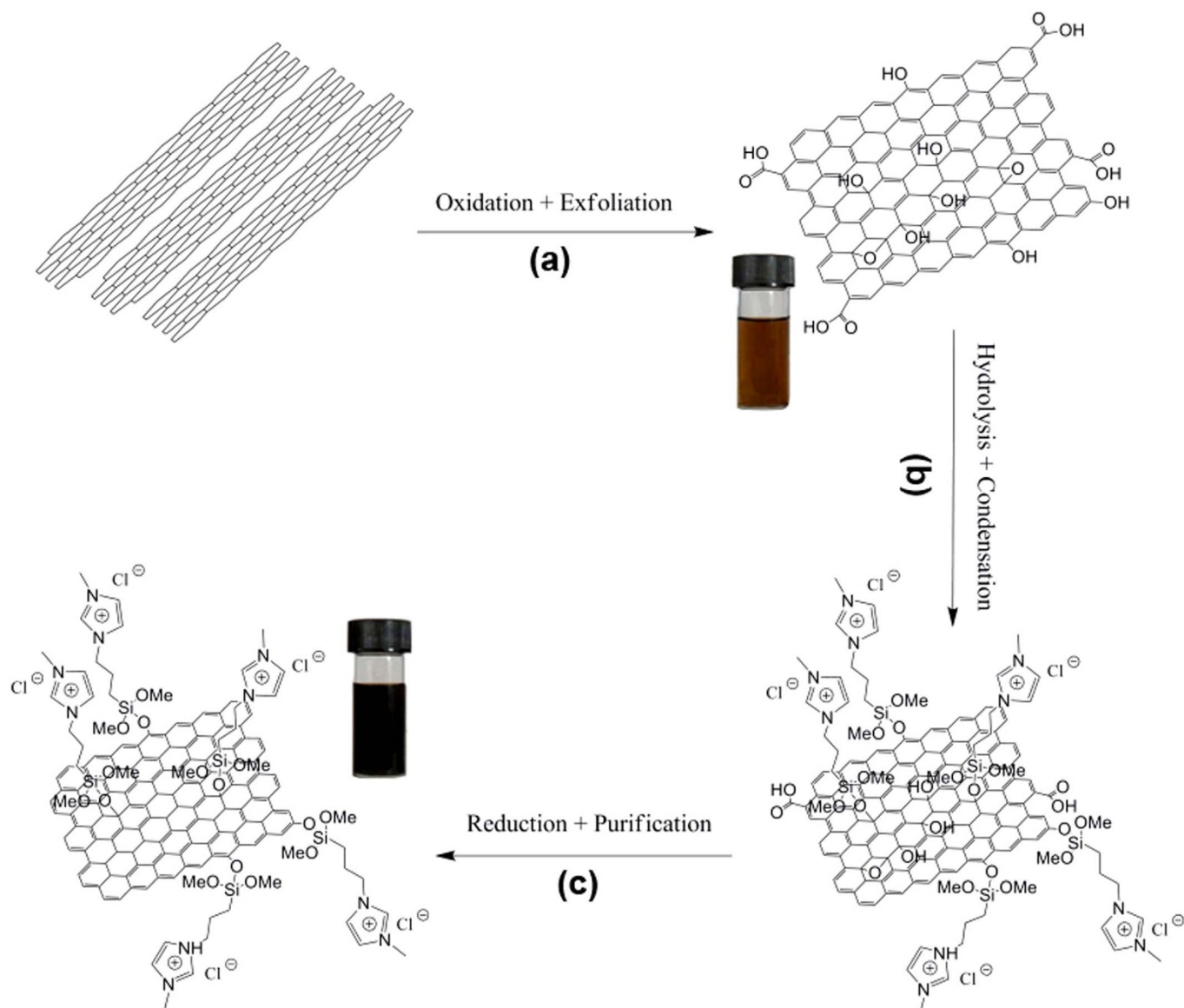


**Figure 1** | Schematics of the chemical reactions between graphite, GO, IL modified GO and reduction.

was designed for wettability control by IL assembly. In our approach, graphene oxide (GO) and 1-Alkyl-3-(3-triethoxysilylpropyl)imidazolium chloride were synthesized and purified. GO surfaces were first modified with an IL monolayer by self-assembly, and then reduced. The cations of IL were anchored on the surface and anions were replaced by an ion exchange method. Wettability of the IL/graphene composite films containing various anions from ion exchange was measured through static contact angle. The effect of solvent systems on ion exchange ratios on the graphene surface has also been investigated. IL possess a combination of unique characteristics including negligible volatility, non-flammability, high thermal stability, wetting and surface forces tenability, which sparked further research and led to its application in surface anti-adhesion, micro-fluidics, and ion-selective electrode.

## Experimental

**Materials.** The graphite flakes were purchased from Sigma-Aldrich, USA. Sulphuric acid, potassium manganate, hydrogen peroxide, hydrazine and ammonia were purchase from Huishi chemical company, Shanghai, China. 1-Alkyl-3-(3-triethoxysilylpropyl)imidazolium chloride ([TSM]Cl) was synthesized and purified according to previously reported procedures<sup>41</sup>. Acetone, isopro-

panol and ethanol all served as analytical reagents. NaPF<sub>6</sub>, Na<sub>2</sub>SO<sub>3</sub>, NaBF<sub>4</sub>, LiN(SO<sub>2</sub>CF<sub>3</sub>)<sub>2</sub> were obtained from Aldrich chemical Co. and Shanghai chemical Co. All reagents were used as received. The polished single crystal silicon wafers were employed as the substrate for contact angle measurement. Silicon wafers were cleaned and hydroxylated in piranha solution (mixture of 7:3 v/v 98% H<sub>2</sub>SO<sub>4</sub> and 30% H<sub>2</sub>O<sub>2</sub>) at 90°C for 30 min before using.

**Synthesis processes and ion exchange.** The synthesis processes of the IL-graphene nanosheets are schematically shown in Figure 1. Graphene oxide (GO) was prepared from expandable graphite powder using a modified Hummers method<sup>42,43</sup>. The procedure was conducted as follows: (a) 1.0 g graphite flakes were preoxidized at 1000°C kept for 30 s. The preoxidized graphite flakes were added to 23 mL H<sub>2</sub>SO<sub>4</sub> in an ice bath while stirring, 3.0 g KMnO<sub>4</sub> was slowly added into the mixture so that the mixture remained at 30°C for 30 min. 46 mL ultrapure water was gradually added. The mixture was further diluted with another 140 mL ultrapure water and 12.5 mL H<sub>2</sub>O<sub>2</sub> solution. The resulting mixture was first washed with ultrapure water until a neutral pH value was achieved. After that, a diluted GO colloid dispersion was obtained by centrifugation and concentration. (b) 10 mg [TSM]Cl

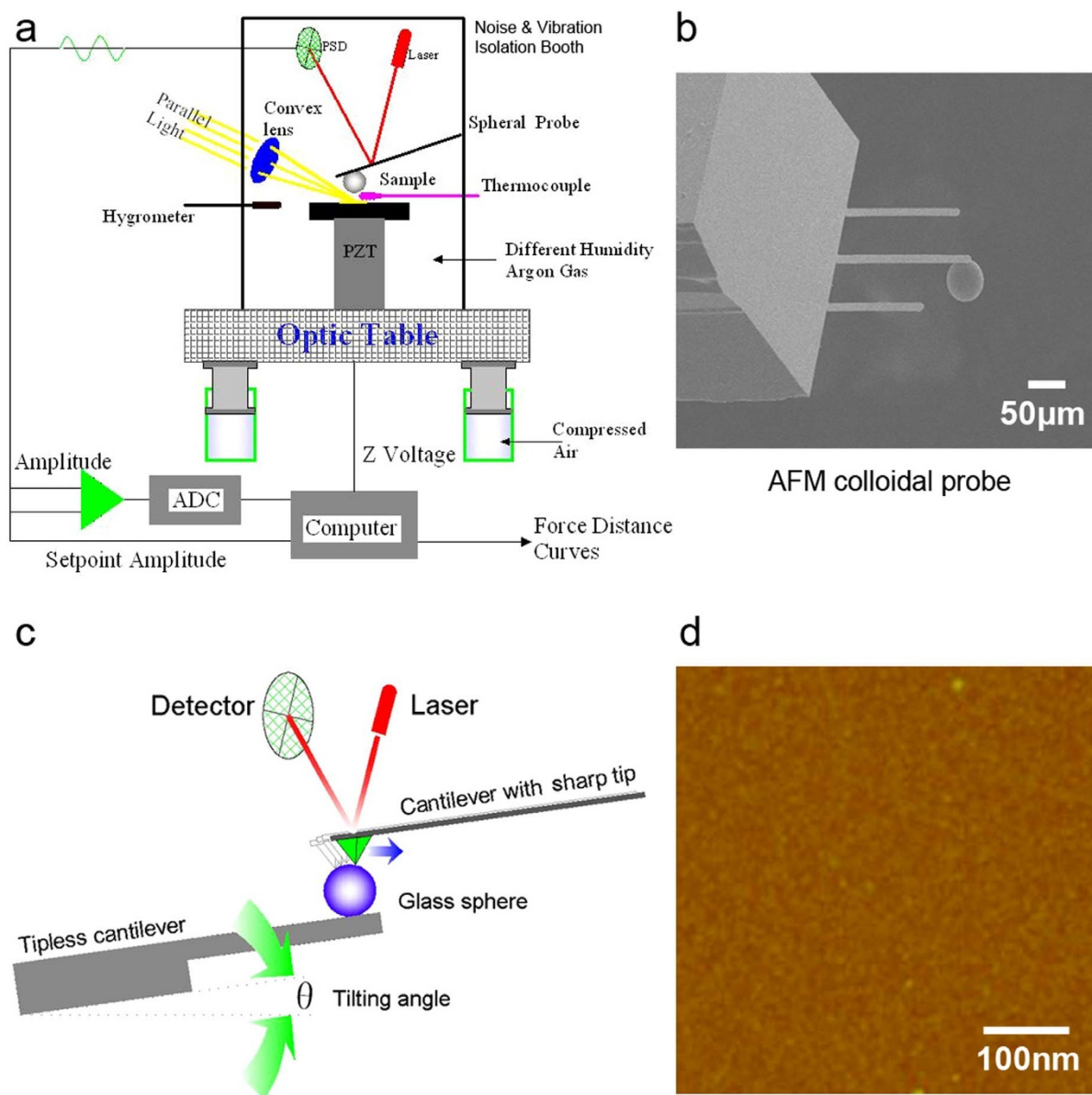


**Figure 2** | Schematic figure of the AFM system used for adhesion measurement (a); SEM image of the colloidal probe in the AFM system (b); Scheme of measuring topography of colloidal probe (c); Topographic image of the colloidal probe (d).

was dissolved in 50 mL of toluene and added into a three-necked round bottom flask. 0.1 g GO sheets were then added into the flask, refluxed at 100 °C for 24 h with magnetic stirring. The hydrolysis of [TSM]Cl and condensation of GO were simultaneously carried out to produce a functional GO solution. (c) 1.0 mM of hydroxybenzotriazole and 1.0 mM of 1-Ethyl-3-(3-dimethylaminopropyl) carbodiimide hydrochloride was dissolved in dimethylformamide. The reaction mixture was stirred at room temperature for 30 minutes. The solution was added one drop at a time into the reaction mixture above and stirred overnight. After that, 2 mL hydrazine and 2 mL ammonia were added dropwise into the dispersion. The mixture was kept at 90 °C for 4 h in an oil bath. Then, the dispersion was washed and centrifuged with ultra-pure water until neutral.

The thin composite films were applied on single crystal silicon using dip-coating technique. The dip-coating technique has been reported in our previous papers<sup>44,45</sup>. Briefly, the film thickness as a function of ionic liquids solution concentration and indicates that the linear increase in film thickness is associated with increase of the

solution concentration<sup>44</sup>. According to this relationship, a desired thickness of film was easily prepared. In this experiment, mechanical performance was evaluated for graphene/ionic liquid-coated surfaces with film thickness of about 1 nm and the main procedure is as follows. The silicon wafers were pulled from solution with the aid of the motorized stage set at a constant speed of 60 μm/s to obtain films of desired thickness. The solution of ionic liquids in ethanol with an appropriate concentration was dip-coated onto pretreated silicon substrates and then dried in nitrogen. The thicknesses of the films after dip-coating were measured by the ellipsometric method.

For ion exchange, five different SAMs of TSM salts having different anions (Cl, PF<sub>6</sub>, SO<sub>3</sub>, BF<sub>4</sub>, N(SO<sub>2</sub>CF<sub>3</sub>)<sub>2</sub>) were investigated as a model system. Measurements of water contact angles could provide quantitative information on the effects of anions on the surface wetting of graphene. The specimens were separately immersed in an aqueous, ethanol and acetone solution of NaBF<sub>4</sub>, NaPF<sub>6</sub>, Na<sub>2</sub>SO<sub>3</sub>, LiN(SO<sub>2</sub>CF<sub>3</sub>)<sub>2</sub> without stirring. Every 2 h, two parallel specimens of each kind were retrieved from the solution, cleaned and dried for the contact angle measurement.

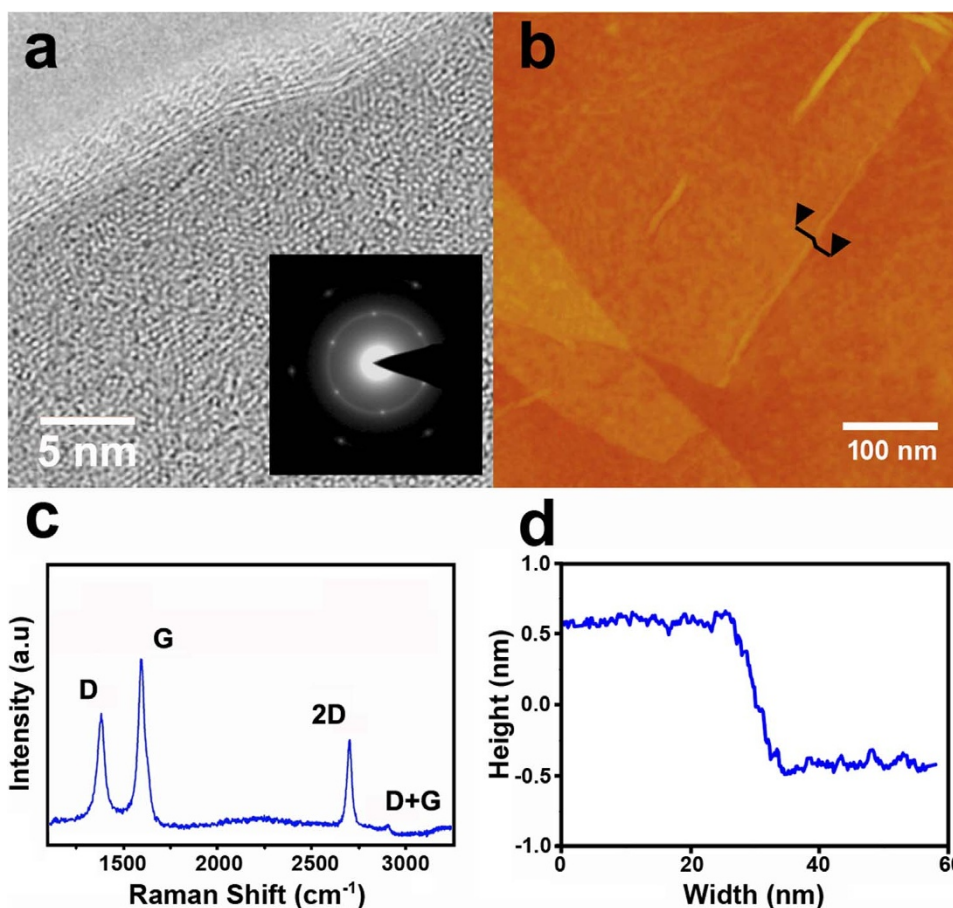


**Figure 3** | FE-TEM image of rGO nanosheets (a), the inset is the SEAD pattern; AFM image of rGO nanosheet (b); Raman spectrum of rGO (c) and Cross-section analysis of AFM image (d).

**Characterization.** The rGO sheet and films were characterized using a field emission transmission electron microscope (Titan S/TEM 80–300, FEI, USA), Raman spectroscopy system (LabRAM HR Raman spectroscopy, Horiba, USA) and Fourier transform infrared spectra (Nicolet 6700, Thermo Scientific Fisher Inc, USA) with a Ge attenuated total reflectance accessory (Harrick Scientific Products Inc, USA). An atomic force/dynamic force microscope (DI3100, Bruker, USA) with contact mode was used to observe the film morphology and surface force measurements. Adhesion behavior of the fabricated films was characterized with an atomic microscope with dynamic force spectroscopy. The influence of relative humidity and temperature on adhesion was studied in a noise and vibration-isolated, environment-controlled booth, as shown in Figure 2a. In order to study the effect of temperature on adhesion, an optic heater was employed to minimize thermal effect on AFM cantilever and PbZrTiO<sub>3</sub> scanner while the local region of the sample surface was heating up. A thermocouple and a hygrometer were used to measure the sample relative humidity and temperature respectively. The temperature ranged from 25 to 400 °C, while the relative humidity ranged from 5 ~ 85%RH during adhesion measurement. To control the contact time independent of the loading rate, a trapezoidal signal from a programmable waveform generator was applied to drive the piezo actuator. A colloidal probe was prepared by gluing glass beads of radius of 20 μm (SRM1003c, radius range from 10 to 22.5 μm, NIST, MD) onto an individual tipless cantilever. The cantilever used in our experiments was etched from single-crystal silicon, gold-coated backside and the force constant of the cantilever was individually calculated using the added mass technique<sup>46,47</sup>. The measured normal force constant of the cantilever was determined to be 0.46–0.56 N/m. A

typical colloidal probe is shown in Figure 2b. The colloidal probe was cleaned by ethanol and then acetone before use. For all measurements the same cantilever was used in this comparative study. Furthermore, to avoid influence of molecules which may transfer to the tip on the AFM/FM experiments, the tip was scanned on a cleaved mica surface to remove these physical adsorbed molecules. The surface topography and microroughness of the colloidal probe was estimated using a cantilever with force constant of 0.1 N/m and a silicon nitride sharp tip under contact mode, as shown in Figure 2c. Figure 2d shows the surface topography of a colloidal tip and root mean square roughness of the tip surface was measured at 0.2 nm. The water contact angle of different specimens was determined using a M295 (Ramé-hart instrument Co. USA). Repeated measurements were averaged for each sample.

## Results and discussion

Figure 3a shows a typical FE-TEM image of rGO. The resulting rGO nanosheet surface was smooth with ripples and the edge was clear and sharp. The selected area electron diffraction (SAED) pattern shows a clear six-fold pattern revealing the crystalline nature of the rGO nanosheet. Detailed surface topography of the rGO nanosheets were obtained by AFM, as shown in Figure 3b. The surface of rGO nanosheets is uniform and smooth with a root-mean-square (RMS) roughness of 0.12 nm. The typical Raman spectrum of rGO is shown in Figure 3c. The D mode appears at approximately 1350 cm<sup>-1</sup>, and the G mode appears at approximately 1580 cm<sup>-1</sup>. G-band arises from the stretching of the C–C bond in graphitic materials, and is related to sp<sup>2</sup> carbon systems. The D-mode is caused by the disordered structure of graphene. The presence of disorder in sp<sup>2</sup>-hybridized carbon systems results in resonance Raman spectra<sup>48</sup>.

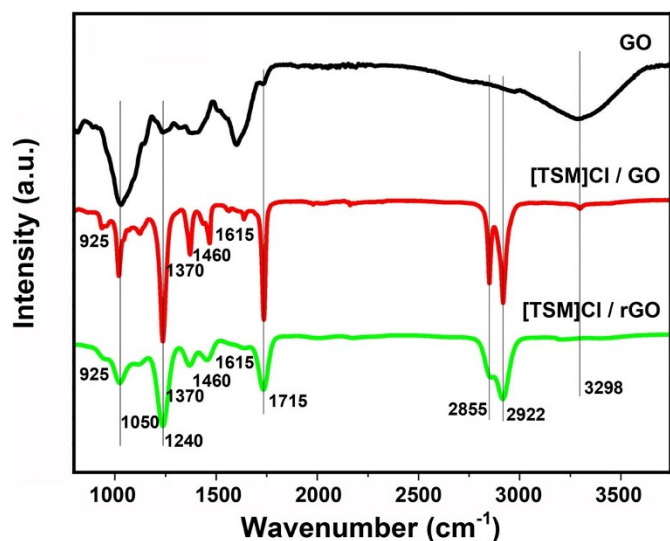


**Figure 4** | FTIR spectra GO, [TSM]Cl modified GO and its reduction.

The other Raman modes are at  $2680\text{ cm}^{-1}$  (2D mode), and  $2925\text{ cm}^{-1}$  (D + G-mode). In conjunction with the G-band, this spectrum is a Raman signature of graphitic  $\text{sp}^2$  materials, and the 2D-band is a second-order two-phonon process and exhibits a strong frequency dependence on the excitation energy. The cross-section

analysis of the high resolution image indicates that the thickness of the rGO sheet is about 0.9 nm which is a bit larger than the theoretical value of 0.34 nm for  $\text{C}_{\text{sp}^2}$  atom network, as shown in Figure 3d. Comparing the FE-TEM observation and AFM cross-section analysis, the graphene nanosheets were consisted primarily of the few-layer with two to three layers.

Grafting of the [TSM]Cl molecules to the graphene surface was further confirmed through attenuated total reflectance-Fourier transform infrared (ATR-FTIR) spectra. As shown in Figure 4, the GO sample exhibits the following characteristic feature of O-H stretching at  $3298\text{ cm}^{-1}$  peak, C-OH vibration appears at  $1240\text{ cm}^{-1}$ , while the epoxy vibration appears at  $1050$  and  $925\text{ cm}^{-1}$ . The peak at  $1370\text{ cm}^{-1}$  might have originated from the C-N bond in the imidazole ring of [TSM]Cl molecules. It can also be seen that the peak frequencies for asymmetric and symmetric methylene vibrations in rGO/[TSM]Cl and rGO/[TSM]Cl, Vas ( $\text{CH}_2$ ) and Vs ( $\text{CH}_2$ ) appear at  $2922$  and  $2855\text{ cm}^{-1}$ , respectively.

Moreover, the exchange process of anions on the silicon surface was confirmed by XPS. Figure 5 shows the XPS of the surface after ion exchange. The XPS survey spectra showed silicon ( $\text{Si } 1s, 2p$ ), chlorine ( $\text{Cl } 2p$ ), carbon ( $\text{C } 1s$ ), nitrogen ( $\text{N } 1s$ ), oxygen ( $\text{O } 1s$ ), and fluorine ( $\text{F } 1s$ ). As shown in Figure 5a, peaks of  $\text{Cl } 2p$  and  $\text{F } 1s$  at  $198.4\text{ eV}$  and  $688.5\text{ eV}$  can be assigned to Cl atoms in [TSM]Cl molecules and  $\text{F } 1s$  spectrum in  $\text{N}(\text{SO}_2\text{CF}_3)_2^-$  anion, respectively. In the  $\text{B } 1s$  and  $\text{Cl } 2p$  spectra that are shown in Figure 5b, there are peaks of  $193.6$  and  $198.7\text{ eV}$ . While the peak at  $164.3\text{ eV}$  is assigned to the  $\text{S } 2p$  spectrum in the  $\text{SO}_3^{2-}$  anion (Figure 5c), the peak that

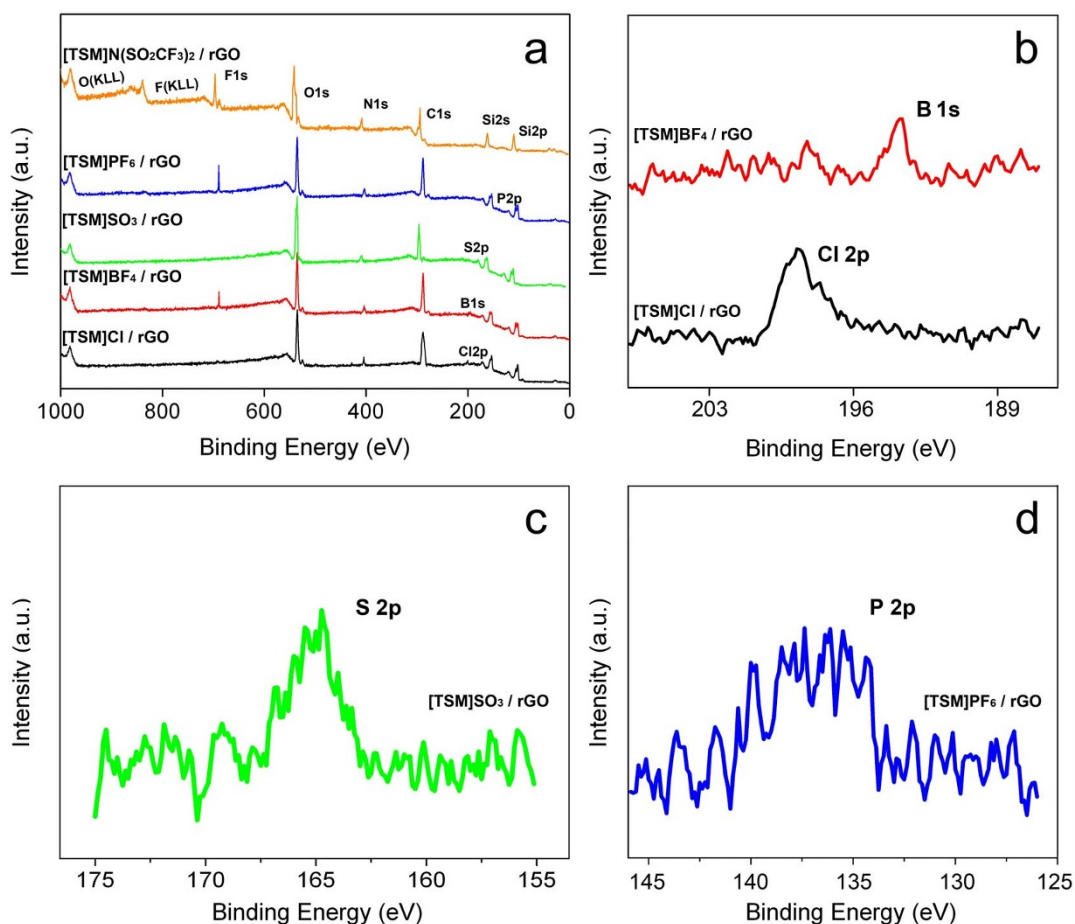


**Figure 5** | X-ray photoelectron spectra of surfaces various anions after ion exchange. (a) Survey spectra of graphene surface various anions; (b) High-resolution spectra between 186 and 206 eV, and peaks of B 1s and Cl 2p were observed in the spectra. (c) High resolution spectrum between 153 eV and 177 eV, and a peak of S 2p was observed in the spectrum. (d) High resolution spectrum between 125 eV and 147 eV, and a peak of P 2p was observed in the spectrum.

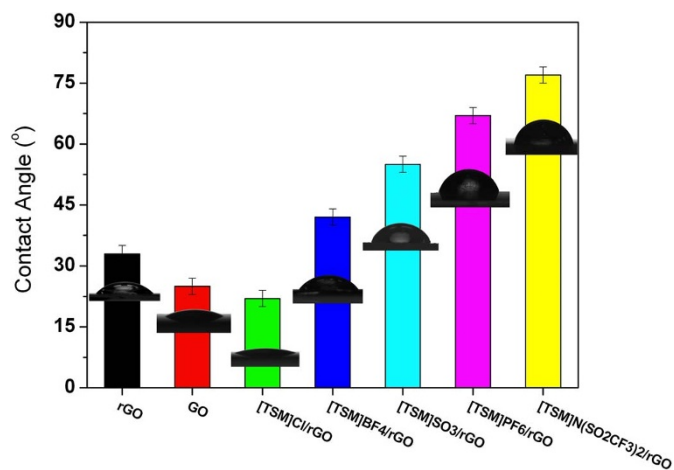


**Figure 6** | Effects of anions on water contact angles of graphene surface.

appears at 136.8 eV can be attributed to the  $P_{2p}$  spectrum in the  $PF_6^-$  anion (Figure 5d).

A histogram of the static contact angle measurement for various graphene surfaces after ion exchange is shown in Figure 6. The contact angle of the graphene surface was measured at  $33^\circ$ . All of the anion-substituted graphene appeared to have higher contact angles than for rGO excluding the  $Cl^-$  anion. Among them, the  $N(SO_2CF_3)_2^-$  anion on graphene exhibited the highest contact angle of  $77^\circ$ . The fluorinated anions had higher contact angles such as  $67^\circ$  for  $PF_6^-$  than those containing other anions, such as  $Cl^-$  ( $22^\circ$ ) and  $SO_3^{2-}$  ( $54^\circ$ ). The tuning of wettability for these ionic liquid/graphene surfaces is probably due to the solvation effect of the anion, as observed in TSM ionic liquids, where the  $Cl^-$  anion has strong hydrogen-bonding interactions with water molecules. This result is quite consistent with that obtained from water-IL partitioning, in which TSM salts of  $PF_6^-$  and  $N(SO_2CF_3)_2^-$  are only partly miscible with water whereas  $Cl^-$ ,  $BF_4^-$  and  $SO_3^{2-}$  salts are water miscible at room temperature. Observation of the TSM ionic liquids/graphene contact angles presents a simple and effective way to quantify the effects of anions on the wetting of TSM-based ionic liquids on graphene surfaces.

The effect of solvent systems on ion exchange ratios on the graphene surface has also been investigated through the anion exchange from  $Cl^-$  to  $N(SO_2CF_3)_2^-$  and three selected solvent systems which including: pure water, ethanol (protic solvent) and acetone (aprotic dipolar solvent). Figure 7 shows that the exchange rate was greatly affected by the solvent systems. The ion exchange was fastest in water from  $Cl^-$  to  $N(SO_2CF_3)_2^-$  and completed in 2 h, while the exchange took 24 h in acetone. Meanwhile, the contact angle of ion exchange in pure water was stable at  $76^\circ$ . In contrast, the contact angle of ion exchange in acetone was approximately  $65^\circ$ . The results indicate that solvent system significantly effect the ion exchange procedure through conversion rate and ionic equilibrium.

The thermal gravimetric curves of Graphite, GO, rGO, rGO/[TSM]Cl, rGO/[TSM]BF<sub>4</sub>, rGO/[TSM]SO<sub>3</sub>, rGO/[TSM]PF<sub>6</sub> and rGO/[TSM]N(SO<sub>2</sub>CF<sub>3</sub>)<sub>2</sub> are shown in Figure 8. No weight loss is detectable for graphite in the testing temperature range. In contrast, weight loss of GO occurs at room temperature and is followed by a dramatic weight loss between the range of 100–160°C which is associated with the dehydration, hydroxyl and carboxyl decomposition. From the TGA curves, It can be observed that GO is not thermally stable and starts to lose mass upon heating below 100°C. Gases such as CO, CO<sub>2</sub>, and steam at 200°C were released

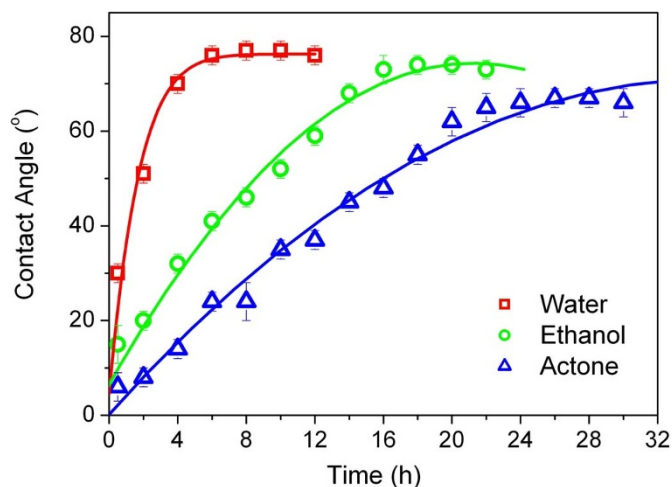


**Figure 7** | Plots of contact angles versus incubation time in pure water, ethanol and acetone.

by thermal decomposition of GO. Similar results were reported by S. Stankovich<sup>49</sup>. The weight loss of rGO is low in the testing temperature range, which indicated that most of the oxygen-containing groups have been removed on GO after reduction. J. Wang and H. Song reported that the thermally labile oxygen functional groups were removed, and the thermal stability of graphene and triethoxysilane-graphene were improved after chemical reduction<sup>50,51</sup>. All the ILs/rGO exhibited high decomposition temperatures, assigned to 240, 270, 290, 330 and 360°C, respectively. The weight loss observed at around 260°C, which was ascribed to the decomposition of the imidazolium cations. Similar results were reported by previous research<sup>52</sup>.

The morphologies of a hydroxylated Si substrate, IL film and IL/rGO composite film were observed by AFM. Compared with the smooth hydroxylated Si substrate (Figure 9a), the IL film exhibits a uniform and densely packed surface structure (Figure 9b). As shown in Figure 9c, the substrate was covered by an IL/rGO composite film, and the rGO nanosheets were embedded in the IL layer. The RMS microroughness of the IL/rGO composite film was measured and averaged approximately 0.5 nm.

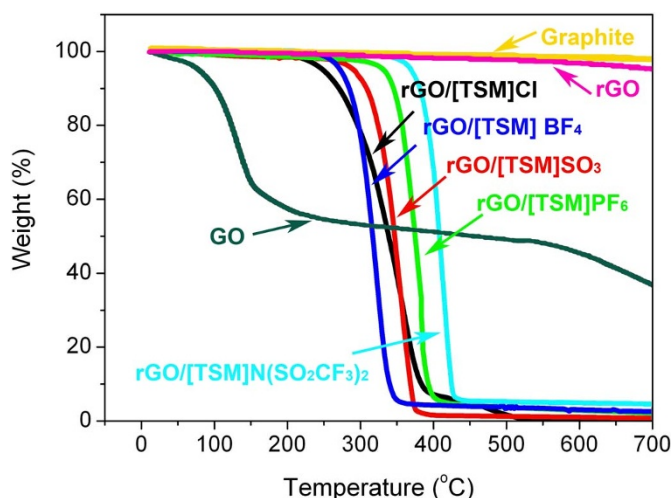


**Figure 8** | TGA curves of the Graphite, GO, rGO, rGO/[TSM]Cl, rGO/[TSM]BF<sub>4</sub>, rGO/[TSM]SO<sub>3</sub>, rGO/[TSM]PF<sub>6</sub>, and rGO/[TSM]N(SO<sub>2</sub>CF<sub>3</sub>)<sub>2</sub> composite films.

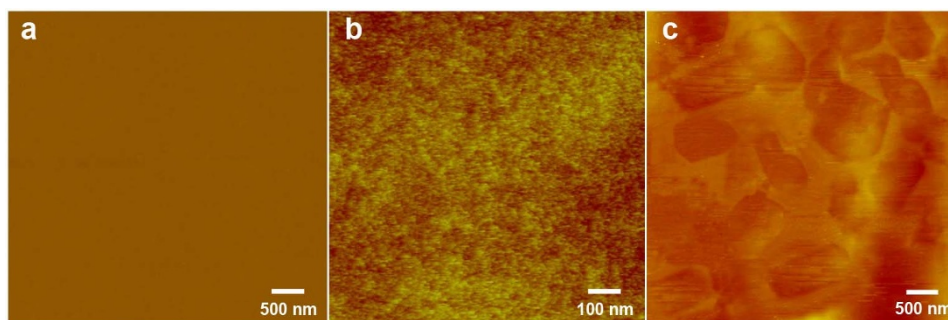


**Figure 9** | AFM morphologies of (a) hydroxylated Si; (b) IL nanofilm; (c) IL/rGO composite nanofilm.

The mechanical properties of [TSM]Cl, rGO, 0.01%rGO/[TSM]Cl, 0.05%rGO/[TSM]Cl, and 0.1%rGO/[TSM]Cl composite films were obtained by colloidal AFM indentation tests. As shown in Figure 10a, Force-distance curves were plotted to identify the relationship between the piezotube displacement and cantilever deflection. Based on the normal spring constant of the colloidal AFM probe, the cantilever deflections were obtained with respect to the displacement of the piezo stage. In the figure, the forces of [TSM]Cl, rGO, 0.01%rGO/[TSM]Cl, 0.05%rGO/[TSM]Cl, and 0.1%rGO/[TSM]Cl nanofilms were measured at 1180, 320, 850, 590, and 440 nN, respectively. This result indicates that rGO nanosheets in the composite film can play a role in enhancing loading-carry capability and reducing elasticity of IL composite films. Figure 10b shows that adhesion of the rGO/[TSM]Cl composite film is dependent on temperature. It is seen that the adhesive force decreased as temperature increased, and with temperature increasing from 50 to 150°C, adhesive force is dropped sharply from 176 to 95 nN. Figure 10c plots the adhesion force for rGO/IL composite films after a surface ionic exchange process. Strong adhesion was observed on the GO coated surface at a temperature of 25°C, at which the adhesive force was 152 nN. After [TSM]Cl ionic liquid molecules self-assembled onto the surface, the adhesive force increased to 183 nN. This indicates that the ionic liquid film exhibited a different adhesion with the GO substrate, because the oxygen containing group was covered by hydrophilic  $\text{Cl}^-$  on the upper layer of the surface. There is a significant discrepancy in the adhesive force of the surface after ion exchange by  $\text{BF}_4^-$ ,  $\text{SO}_3^{2-}$ ,  $\text{PF}_6^-$ ,  $\text{N}(\text{SO}_2\text{CF}_3)_2^-$  in turn. Among them,  $\text{N}(\text{SO}_2\text{CF}_3)_2^-$  exhibited the lowest adhesive force, about 29 nN, while the adhesive forces of  $\text{BF}_4^-$ ,  $\text{SO}_3^{2-}$  and  $\text{PF}_6^-$  appeared at 115, 97 and 38 nN, respectively. The tendency of the friction force agrees well with the change in contact angle measurements, which correlates with the surface energy. The

influence of temperature on surface adhesion is shown in this figure. The adhesive force of these films significantly decreased while temperature increased to 200°C. Compared with results shown in Figure 8, the pure IL film and rGO/IL composite films are stable without decomposition. The drop in adhesive force is a result of desorption of water molecules and the corresponding decrease of water menisci contribution. In high temperature, the adhesive forces between the colloid probe and sample surface may be due to electrostatic force and diversity of ionic charge. The results indicated that surface ions can be quantitatively determined by their adhesive force, which might provide a novel and simple technique for anion detection at the single molecule scale.

## Conclusions

In summary, IL molecules were self-assembled onto the surface, and then the anions were replaced to the outermost layer by an ion exchange method to minimize the impact of other ions. The self-assembly and ion exchange process on the graphene surface were confirmed by FTIR and XPS. Wettability of graphene was adjusted by the formation of various ionic surfaces combining IL SAMs with ion exchange. The effect of wettability on the surface bearing various anions was studied systematically. The effect of solvent systems on ion exchange ratios on the graphene surface has also been investigated. The results indicated that anions played a great role in determining graphene surface properties and sensitivity to solvent systems. Mechanical properties of the graphene/IL composite film were investigated by high temperature colloidal probe AFM and nanoindentation. Furthermore, surface elasticity and adhesion can be quantitatively determined by the counter-anions on the surface. It provides a novel and simple technique for applications towards anion detection and microfluidics.

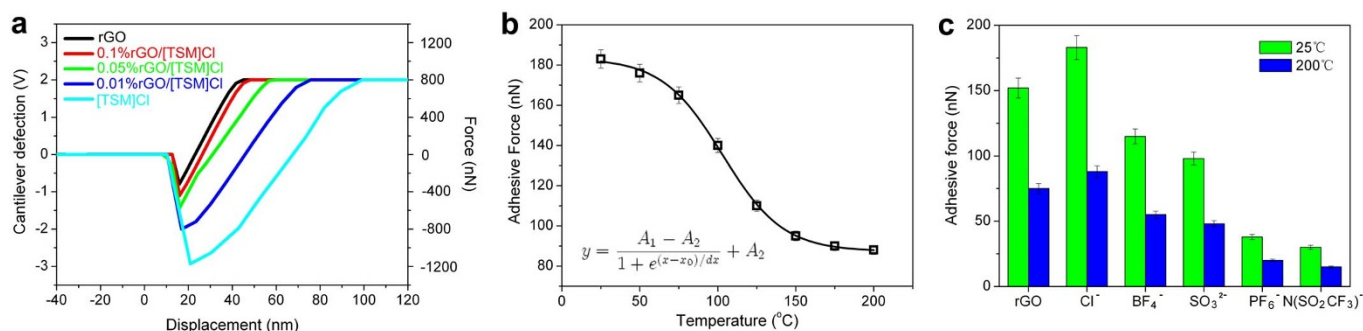


**Figure 10** | Force-distance curves for [TSM]Cl, rGO, 0.01%rGO/[TSM]Cl, 0.05%rGO/[TSM]Cl, and 0.1%rGO/[TSM]Cl composite film surfaces (a); Dependence on temperature of adhesion for the rGO/[TSM]Cl composite film (b); Adhesive forces between the colloid probe and the surfaces of rGO/IL composite films (c).



1. Kim, K. *et al.* Electric property evolution of structurally defected multilayer graphene. *Nano Lett.* **8**, 3092–3096 (2008).
2. Song, J. *et al.* A general method for transferring graphene onto soft surfaces. *Nat Nanotechnol.* **8**, 356–362 (2013).
3. Fan, X., Jiao, G., Zhao, W., Jin, P. & Li, X. Magnetic Fe<sub>3</sub>O<sub>4</sub>-graphene composites as targeted drug nanocarriers for pH-activated release. *Nanoscale.* **5**, 1143–1152 (2013).
4. Novoselov, K. S. *et al.* Electric field effect in atomically thin carbon films. *Science.* **306**, 666–669 (2004).
5. Lee, C., Wei, X. D., Kysar, J. W. & Hone, J. Measurement of the elastic properties and intrinsic strength of monolayer graphene. *Science.* **321**, 385–388 (2008).
6. Geim, A. K. Graphene: status and prospects. *Science.* **324**, 1530–1534 (2009).
7. Jiao, L. Y., Zhang, L., Wang, X. R., Diankov, G. & Dai, H. J. Narrow graphene nanoribbons from carbon nanotubes. *Nature.* **458**, 877–880 (2009).
8. Geim, A. K. & Novoselov, K. S. The rise of graphene. *Nat Mater.* **6**, 183–190 (2007).
9. Chen, W., Yan, L. & Bangal, P. R. Chemical reduction of graphene oxide to graphene by sulfur-containing compounds. *J Phys Chem C.* **114**, 19885–19890 (2010).
10. Tung, V. C., Allen, M. J., Yang, Y. & Kaner, R. B. High-throughput solution processing of large-scale graphene. *Nat Nanotechnol.* **4**, 25–29 (2009).
11. Li, X., Cai, W., Piner, R. D. & Stadermann, F. J. Large-area synthesis of high-quality and uniform graphene films on copper foils. *Science.* **324**, 1312–1314 (2009).
12. Li, B., Cao, X. H., Ong, H. G., Cheah, J. W. & Zhou, X. Z. All-carbon electronic devices fabricated by directly grown single-walled carbon nanotubes on reduced graphene oxide electrodes. *Adv Mater.* **22**, 3058–3061 (2010).
13. Yang, N., Zhai, J., Wang, D., Chen, Y. & Jiang, L. Two-dimensional graphene bridges enhanced photoinduced charge transport in dye-sensitized solar cells. *ACS Nano.* **4**, 887–894 (2010).
14. Arco, L. G., Zhang, Y. & Schlenker, C. W. Continuous, highly flexible, and transparent graphene films by chemical vapor deposition for organic photovoltaics. *ACS Nano.* **4**, 2865–2873 (2010).
15. Zhao, J. P., Pei, S. P. & Ren, W. C. Efficient preparation of large-area graphene oxide sheets for transparent conductive films. *ACS Nano.* **4**, 5245–5252 (2010).
16. Kasry, A., Kuroda, M. A. & Martyna, G. J. Chemical doping of large-area stacked graphene films for use as transparent, conducting electrodes. *ACS Nano.* **4**, 3839–3844 (2010).
17. Qi, X. Y., Pu, K. Y. & Li, H. Amphiphilic graphene composites. *Angew Chem Int Ed.* **49**, 9426–9429 (2010).
18. Mo, Y., Yang, M., Lu, Z. & Huang, F. Preparation and tribological performance of chemically-modified reduced graphene oxide/polyacrylonitrile composites. *Composites A.* **54**, 153–158 (2013).
19. Ang, P. K., Chen, W. A. & Wee, S. Solution-gated epitaxial graphene as pH sensor. *J Am Chem Soc.* **130**, 14392–14393 (2008).
20. Dong, X. C., Shi, Y. M. & Huang, W. Electrical detection of DNA hybridization with single-base specificity using transistors based on CVD-grown graphene sheets. *Adv Mater.* **22**, 1649–1653 (2010).
21. Dato, A., Radmilovic, V., Lee, Z. H., Phillips, J. & Frenklach, M. Substrate-free gas-phase synthesis of graphene sheets. *Nano Lett.* **8**, 2012–2016 (2008).
22. Reina, A. *et al.* Large area, few-layer graphene films on arbitrary substrates by chemical vapor deposition. *Nano Lett.* **9**, 30–35 (2009).
23. Hsu, P. L. *et al.* Epitaxial graphene transistors on SiC substrates. *IEEE Transactions on Electron Devices.* **55**, 2078–2085 (2008).
24. Pei, S. & Cheng, H. The reduction of graphene oxide. *Carbon.* **50**, 3210–3228 (2012).
25. Safran, S. A. & Hamann, D. R. Long-range elastic interactions and staging in graphite intercalation compounds. *Phys Rev Lett.* **42**, 1410–1416 (1979).
26. Prasher, R. Graphene spreads the heat. *Science.* **328**, 185–186 (2010).
27. Park, S. & Ruoff, R. S. Chemical methods for the production of graphemes. *Nat Nanotechnol.* **4**, 217–224 (2009).
28. Allen, M. J., Tung, V. C. & Kaner, R. B. Honeycomb carbon: a review of graphene. *Chem Rev.* **110**, 132–145 (2010).
29. Subrahmanyam, K. S., Ghosh, A., Gomathi, A., Govindaraj, A. & Rao, C. N. R. Covalent and noncovalent functionalization and solubilization of graphene. *Nanosci. Nanotechnol Lett.* **1**, 28–31 (2009).
30. Rao, C. N. R., Sood, A. K., Voggu, R. H. & Subrahmanyam, K. S. Quenching of fluorescence of aromatic molecules by graphene due to electron transfer. *J Phys Chem Lett.* **1**, 572–580 (2010).
31. Raj, R., Maroo, S., Maroo, C. & Wang, E. N. Wettability of graphene. *Nano Lett.* **13**, 1509–1515 (2013).
32. Marcus, C. M., Williams, J. R. & Churchill, H. US20110089404A1. April 21, 2011.
33. Wen, H. *et al.* Engineered redox-responsive PEG detachment mechanism in PEGylated nano-graphene oxide for intracellular drug delivery. *Small.* **8**, 760–769 (2012).
34. Frank, G. *et al.* Development of an universal stress sensor for graphene and carbon fibres. *Nat Commun.* **2**, 255 (2011).
35. Mo, Y., Huang, F., Pan, S. & Huang, F. Fabrication and Adhesion Measurement of a Nanotextured Surface with Ionic Liquid Monolayers. *J. Phys. Chem. C.* **115**, 10125–10130 (2011).
36. Mo, Y. & Bai, M. Preparation and Adhesion of a Dual-Component Self-Assembled Dual-Layer Film on Silicon by a Dip-Coating Nanoparticles Method. *J. Phys. Chem. C.* **112**, 11257–11264 (2008).
37. Mo, Y., Bo, Y., Zhao, W. & Bai, M. Microtribological properties of molecularly thin carboxylic acid functionalized imidazolium ionic liquid film on single-crystal silicon. *Applied Surface Science.* **255**, 2276–2283 (2008).
38. Tamailarasan, P. & Ramaprabhu, S. Carbon Nanotubes-Graphene-Solidlike Ionic Liquid Layer-Based Hybrid Electrode Material for High Performance Supercapacitor. *J. Phys. Chem. C.* **116**, 14179–14187 (2012).
39. Lee, J., Lee, T., Song, H., Cho, J. & Kim, B. Ionic liquid modified graphene nanosheets anchoring manganese oxide nanoparticles as efficient electrocatalysts for Zn-air batteries. *Energy Environ. Sci.* **4**, 4148–4154 (2011).
40. Pu, J. *et al.* Preparation and Tribological Study of Functionalized Graphene-IL Nanocomposite Ultrathin Lubrication Films on Si Substrates. *J. Phys. Chem. C.* **115**, 13275–13284 (2011).
41. Mehnert, C. P., Cook, R. A., Dispenziere, N. C. & Afeworki, M. Supported ionic liquid catalysis - a new concept for homogeneous hydroformylation catalysis. *J Am Chem Soc.* **124**, 12932–12933 (2002).
42. Hummer, W. S. & Offerman, R. E. Preparation of graphitic oxide. *J Am Chem Soc.* **80**, 1339–1339 (1958).
43. Mo, Y., Chau, A., Wan, Y., Lu, Z. & Huang, F. Fabrication and tribological properties of a multiply-alkylated cyclopentane/reduced graphene oxide composite ultrathin film. *Carbon.* **65**, 261–268 (2013).
44. Hutter, J. L. & Bechhoefer, J. Calibration of atomic-force microscope tips. *Rev. Sci. Instrum.* **64**, 1868 (1993).
45. Mo, Y., Zhao, W., Zhu, M. & Bai, M. Nano/Microtribological Properties of Ultrathin Functionalized Imidazolium Wear-Resistant Ionic Liquid Films on Single Crystal Silicon. *Tribology Letters* **32**, 143–151 (2008).
46. Mo, Y., Pu, J. & Huang, F. Dynamic forces of ionic liquid nano-droplets measured by atomic force microscope. *Colloids and Surfaces A* **429**, 19–23 (2013).
47. Mo, Y., Wang, Y., Pu, J. & Bai, M. Precise positioning of lubricant on surface using local anodic oxide method. *Langmuir.* **25**, 40–42 (2009).
48. Kang, H., Kulkarni, A., Stankovich, S., Ruoff, R. S. & Baik, S. Restoring electrical conductivity of dielectrophoretically assembled graphite oxide sheets by thermal and chemical reduction techniques. *Carbon.* **47**, 1520–1525 (2009).
49. Stankovich, S. *et al.* Synthesis of graphene-based nanosheets via chemical reduction of exfoliated graphite oxide. *Carbon* **45**, 1558–1565 (2007).
50. Wang, J. *et al.* Synthesis, Mechanical, and barrier properties of LDPE/graphene nanocomposites using vinyl triethoxysilane as a coupling agent. *J Nanopart Res* **13**, 869–878. (2011).
51. Song, H., Li, N., Li, Y., Min, C. & Wang, Z. Preparation and tribological properties of graphene/poly(ether ether ketone) nanocomposites. *J Mater Sci* **47**, 6436–6443. (2012).
52. Peng, Y. *et al.* Synthesis of carbon - PtAu nanoparticle hybrids originating from triethoxysilane-derivatized ionic liquids for methanol electrooxidation and the catalytic reduction of 4-nitrophenol. *J. Mater. Chem. A* **1**, 9257–9263. (2013).

## Acknowledgments

This work was funded by the National Natural Science Foundation of China under grant No. 51205070 and the Natural Science Foundation of Guangxi under grant No. 2012GXNSFBA053023 and 2013GXNSFAA019030.

## Author contributions

Y.M. and Y.W. wrote the main manuscript text. Y.M. and F.H. design experimental procedure. Y.W. run AFM force calibration and A.C. contact angle measurement and data analysis. Y.M. draw the figure 1–6, Y.F. and A.C. draw the figure 7–10. All authors reviewed the manuscript.

## Additional information

**Competing financial interests:** The authors declare no competing financial interests.

**How to cite this article:** Mo, Y., Wan, Y., Chau, A. & Huang, F. Graphene/Ionic Liquid Composite Films and Ion Exchange. *Sci. Rep.* **4**, 5466; DOI:10.1038/srep05466 (2014).



This work is licensed under a Creative Commons Attribution-NonCommercial-ShareAlike 4.0 International License. The images or other third party material in this article are included in the article's Creative Commons license, unless indicated otherwise in the credit line; if the material is not included under the Creative Commons license, users will need to obtain permission from the license holder in order to reproduce the material. To view a copy of this license, visit <http://creativecommons.org/licenses/by-nc-sa/4.0/>